POLITECNICO DI TORINO
Repository ISTITUZIONALE

Modeling of daytime radiative cooling enhanced vapor-compression refrigeration systems

Original
Modeling of daytime radiative cooling enhanced vapor-compression refrigeration systems / Forte, D., Belotti, C., Pattelli, L., Morciano, M., Chiavazzo, E., Asinari, P., Fasano, M.. - In: ENERGY. - ISSN 0360-5442. - ELETTRONICO. - 340:(2025). [10.1016/j.energy.2025.139101]

Availability:
This version is available at: 11583/3004936 since: 2025-11-07T08:29:01Z

Publisher:
Elsevier

Published
DOI:10.1016/j.energy.2025.139101

Terms of use:

This article is made available under terms and conditions as specified in the corresponding bibliographic description in the repository

Publisher copyright

(Article begins on next page)

16 October 2026

Energy 340 (2025) 139101

Contents lists available at ScienceDirect

Energy

journal homepage: www.elsevier.com/locate/energy

Modeling of daytime radiative cooling enhanced vapor-compression refrigeration systems

Davide Forte [a], Claudio Belotti [b], Lorenzo Pattelli [c], Matteo Morciano [a], Eliodoro Chiavazzo [a], Pietro Asinari [a,c], Matteo Fasano [a,*]

[a] Department of Energy, Politecnico di Torino, Corso Duca degli Abruzzi 24, Torino, 10129, Italy
[b] Istituto Nazionale di Ottica (CNR-INO), Via Madonna del Piano 10, Sesto Fiorentino, Firenze, 50019, Italy
[c] Istituto Nazionale di Ricerca Metrologica, Strada delle Cacce 91, Torino, 10135, Italy

ARTICLE INFO

Dataset link: https://doi.org/10.5281/zenodo.14938900

Keywords:
Daytime radiative cooling
Vapor compression refrigeration system
Building
Sustainability
Heat and mass transfer

ABSTRACT

Daytime Radiative Cooling (DRC) technologies use surfaces with tailored spectral properties to dissipate heat through the atmospheric transparency window towards outer space, even under direct sunlight. This study develops a transient simulation model to assess the energy-saving potential of integrating DRC materials into a typical vapor-compression refrigeration system (VCRS) for a residential building. The system employs flat-plate radiative panels coated with DRC material to cool a heat transfer fluid in a closed-loop circuit. This cooled liquid then reduces the temperature of the VCRS refrigerant via a supplementary heat exchanger located downstream of the air-cooled condenser, thereby enhancing the seasonal energy efficiency ratio (SEER) and reducing energy consumption. A parametric analysis examines key parameters, including radiative panel area, subcooler size, and panel fluid flow rate. The system is simulated for Las Vegas, Riyadh, Madrid, and Turin using experimental hourly meteorological data to capture the spectrally varying effects of atmospheric radiation. Moreover, the performance of different DRC materials is evaluated by comparing spectral selective and broadband emitters with two commercial options. Results show significant energy savings in hot, arid climates—46.1 $kW\,h_{el}\,m_{DRC}^{-2}$ in Riyadh and 37.5 $kW\,h_{el}\,m_{DRC}^{-2}$ in Las Vegas—and up to a 10.1 % reduction in electric energy consumption.

1. Introduction

Electricity use in the building sector has grown rapidly, reaching 37 % of total energy demand in 2023 and projected to reach 50 % by 2050 [1]. Space cooling is the main driver of this growth, accounting for about 20 % of total electricity consumption in buildings and increasing faster than any other end use in this sector [2]. The escalation in cooling demand can be ascribed to the rising population and increasing income levels [3], as well as to global warming, which exceeded 1.5 °C above pre-industrial level for the first time in 2024 [4]. According to the International Energy Agency, space cooling was responsible for approximately 1 billion tonnes of CO_2 emissions resulting from electricity consumption in 2022, constituting 2.7 % of global energy-related CO_2 emissions [5,6]. In this context, radiative cooling technologies present a potentially valuable solution for mitigating the environmental impacts of systems devised to keep thermal comfort (e.g. textiles, space cooling systems) [7,8].

Radiative cooling enables the dissipation of heat directly to outer space by exploiting the atmospheric transparency window, a spectral range (8–13 μm) in which the atmosphere exhibits high transparency to thermal radiation emitted by terrestrial objects with a temperature close to Earth surface temperature (~ 300 K). However, the optical transmissivity of the atmospheric window is influenced by various atmospheric factors, including humidity, cloud coverage, and aerosol concentration [9]. Radiative cooling technologies can be classified as renewable, as they harness the coldness of outer space as a heat sink [10], and as passive technologies, since they do not require any external energy input to operate, aside from potential energy required for circulating a heat transfer fluid (HTF) in certain applications.

While nighttime radiative cooling is known since ancient times [11] and has been extensively studied [12], daytime radiative cooling (DRC) has been experimentally demonstrated for the first time only in recent times [13]. The principal challenge of DRC lies in engineering the optical properties of the emitter to simultaneously achieve high emissivity within the atmospheric window and high reflectivity across the solar spectrum (300 nm to 2.5 μm), thereby minimizing heat absorption from solar irradiance. Recent advancements in material fabrication

* Corresponding author.
E-mail address: matteo.fasano@polito.it (M. Fasano).

https://doi.org/10.1016/j.energy.2025.139101
Received 5 March 2025; Received in revised form 18 August 2025; Accepted 29 October 2025
Available online 1 November 2025
0360-5442/© 2025 The Authors. Published by Elsevier Ltd. This is an open access article under the CC BY license (http://creativecommons.org/licenses/by/4.0/).

have enabled the development of structures capable of significant cooling performance even under direct sunlight. DRC has been achieved using nanophotonic materials composed of multiple micrometer-thick layers of different materials deposited on a metallic reflector, often incorporating artificially designed microstructures [13–15]. Also micro- and nanoparticle-based materials have demonstrated effective DRC properties [16,17]. Polymer-based materials, implemented either as polymeric films on metallic reflectors or as micro- and nano-porous polymers, have also been shown to achieve DRC [18,19]. Additionally, other classes of advanced material systems have exhibited DRC capabilities [20].

The analysis of publication trends indicates that research in DRC is rapidly advancing and that, within the building sector, researchers focus is split between passive radiative cooling surfaces and active hybrid systems, including air-based, water-based, HVAC-integrated, solar photovoltaic/solar thermal-integrated configurations [21,22]. Passive DRC materials, typically applied to building roofs and walls, function by minimizing solar heat gain and enhancing thermal re-radiation. This dual action contributes to lower average internal building temperatures, thereby reducing the energy demand for cooling. DRC materials can mitigate the urban heat island effect by redirecting accumulated heat in urban areas to outer space, reducing street-level heat buildup, and they have proven to be more effective than cool roofs in doing that [23,24]. The integration of DRC materials into residential and industrial roofing systems has been extensively investigated in the literature [25–31]. These studies consistently demonstrate that DRC-integrated roofs significantly reduce cooling energy demand compared to conventional roofing materials. However, in heating-dominated climates, the energy savings achieved during the cooling season are partially or entirely offset by increased heating demands during colder periods, resulting in minimal or even adverse overall energy performance [27,28,30]. To address this limitation, innovative solutions have been developed, including materials that can alternate between radiative cooling and solar heating by flipping their surface orientation [32,33] and self-adaptive materials capable of deactivating the DRC function when triggered by environmental stimuli [34]. These advancements aim to optimize the year-round performance of DRC materials across different climatic conditions.

Active DRC systems, which transfer the cooling effect to a flowing thermal fluid, solve heating penalty issues, as the cooling effect can be stopped by switching off fluid circulation. Also, when integrated with other active systems, as air conditioning (AC) devices, DRC hybrid systems can achieve higher cooling rates than passive DRC systems for the same surface area [35]. Goldstein et al. [36] demonstrated that coupling a large array of DRC panels, covering 60 % of an office building roof, with a vapor-compression refrigeration system (VCRS) can reduce electricity consumption by 21 % during the hot season under Las Vegas climate conditions. An experimental setup at Fort Moore showed that DRC panels reduced electricity consumption for space cooling by 22 % in a canteen facility when functioning as a subcooler for the AC system and by 42 % in a data closet room when used in remote condenser mode [37]. Yuan et al. [38] found that cold water produced by DRC panels on a single-family building roof and delivered through a radiant cooling floor yielded 72 % energy savings in Denver by displacing the conventional AC system. Xu et al. [39] reported that pre-cooling air entering an HVAC system with DRC materials reduced cooling energy consumption by approximately 10 % in most climates. Other studies have further shown that integrating water-based DRC panels with conventional HVAC systems can achieve around 22 % energy savings, rising to 26–46 % when combined with cold storage, depending on location [40,41].

Another approach to space thermal management involves hybrid solar heating–nighttime radiative cooling (SH/NRC) systems. Fiorentini et al. [42] used SH/NRC modules to precondition air entering an HVAC system, reducing the building energy consumption. González-Cruz and Krüger [43] employed a water-based SH/NRC system with cold storage and radiative internal modules for space heating and cooling, while Vilà et al. [44] adopted a similar setup but used cold water stored at night to enhance a VCRS for domestic use. Furthermore, Hu et al. [45] designed a photovoltaic-SH/NRC system that integrates thermal energy harvesting with electricity generation for multifunctional applications.

Even if the interest towards DRC-integrated AC systems is growing, to the best knowledge of the authors, the scientific literature exploring the energy-saving potential of DRC materials applied to residential VCRSs is limited. Additionally, few studies have developed dynamic models capable of simulating the transient operation of radiative cooling panels over entire cooling seasons. Therefore, an in-depth investigation of the transients associated with this technology is essential for its proper characterization and a fair assessment of its potential. This study is focused on the development of a dynamic model capable of simulating a DRC-enhanced VCRS under varying operating and meteorological conditions. The DRC materials are applied as a film on flat panels, designed to cool an intermediate HTF by radiating excess heat to the sky, even during periods of high solar irradiance. The cooled intermediate fluid provides additional cooling to the refrigerant within the VCRS via an auxiliary heat exchanger, referred to as a subcooler [46]. A sensitivity analysis is conducted to evaluate the influence of key operational parameters, including the surface area of the DRC panels, the size of the subcooler, and the flow rate of the HTF circulating within the panels.

The system is further tested under the meteorological conditions of four locations: Riyadh (Saudi Arabia), Las Vegas (USA), Madrid (Spain), and Turin (Italy), considering two building energy classes. Realistic climatic data for June, July, and August 2023, obtained from the ERA5 database [47], are used as model inputs. Lastly, the system performance is assessed using different DRC emissivity profiles, including both idealized and commercially available materials.

This study could contribute significantly to the design and optimization of DRC-based systems for building thermal management, providing valuable insights into both the strengths and limitations of this technology. Furthermore, the findings demonstrate how DRC technology could play a pivotal role in the development of more energy-efficient and environmentally sustainable buildings, particularly in hot and dry climates.

2. Methods and model implementation

To assess the energy saving potential of DRC-assisted VCRSs in residential buildings, a lumped-parameters model was developed and dynamically simulated in *Simscape* [48], a MATLAB Simulink environment that allows to create multiphysics models. Different *Simscape* libraries were adopted to build the model. The blocks from these libraries were, then, properly connected in order to define the entire physical system. The model can be conceptually divided in three parts: (i) building, (ii) AC system, comprising the VCRS, fan-coil unit (FCU), water distribution network and additional subcooler, and (iii) DRC-coated panels. A representation of plant schematic is displayed in Fig. 1.

2.1. Building

The case study considered in this model is that of a single family building composed of two conditioned stories (with a net surface of 174 m^2) and a non-conditioned attic. The thermal transmittances of building components, including external walls, slabs, roof, floors, windows, and doors, were determined based on data from Tabula database [49]. Two distinct building categories were analyzed: a building constructed between 1991 and 2005 (denoted as the *Standard building*) and one constructed post-2005 (denoted as the *Modern building*). Using the thermal transmittances data, appropriate stratigraphies were developed employing conventional materials in the construction industry [50].

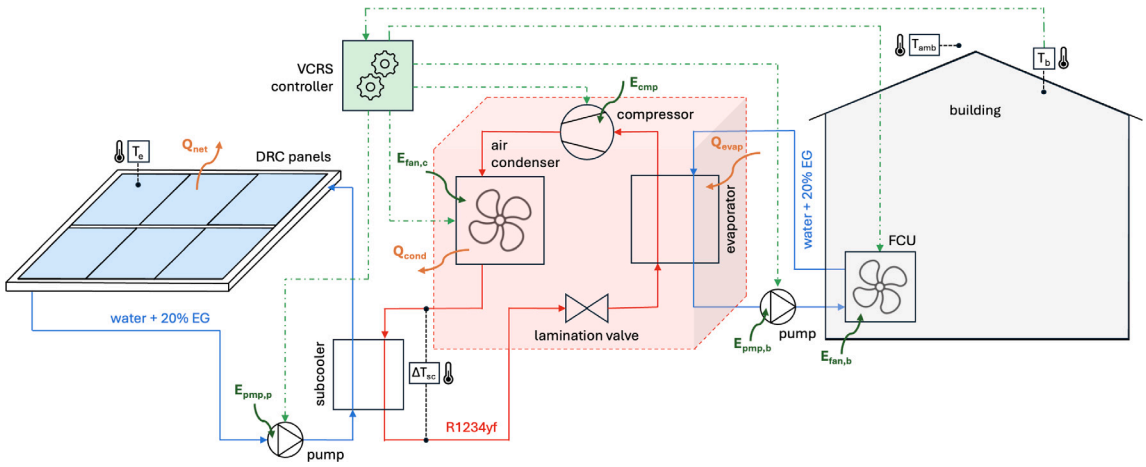

Fig. 1. Schematic of the model developed in *Simscape* environment of the DRC panels coupled to the AC system of a building. The entering and exiting flows of electric energy (in green color) and the thermal fluxes (in orange color) are also represented.

The thermal loads affecting the building in the model included heat transfer through external surfaces, solar radiation absorbed by opaque surfaces and transmitted through windows, heat generated by internal sources, and ventilation heat exchange arising from both infiltration and intentional ventilation. For simplicity, thermal re-radiation was assumed to occur exclusively on the roof, while its effect on external walls was neglected. The conditioned volume of the building was modeled as a single entity, disregarding the thermal effects of internal masses, such as interior walls, which were not simulated. The unconditioned attic is separated from the conditioned space by an upper slab. The building facades are aligned with the four cardinal directions, and the roof was assumed to be flat and perfectly horizontal. The model also accounts for changes in roof albedo due to the presence of the DRC-coated panels. A detailed description of the building thermal and optical properties, along with its detailed stratigraphy and the equations implemented in the model can be found in the Supplementary Material, Section S1.

2.2. AC system

The building AC system comprises a VCRS, an internal FCU, and the additional condenser subcooler. To ensure full model replicability, the detailed geometry, operating parameters, and implementation of all components in *Simscape* environment are included in the Supplementary Material, Section S2.

2.2.1. Vapor-compression refrigeration system

The building cooling demand was met by an air–water VCRS using R1234yf, a modern refrigerant with low global warming potential [51]. The VCRS comprises an air-cooled condenser (modeled as a tube-fin heat exchanger), a volumetric compressor, an evaporator (extracting heat from the FCU circuit and modeled as a shell-and-tube heat exchanger), a thermostatic expansion valve, and a small refrigerant fluid reservoir. The additional DRC-driven subcooler was installed downstream of the condenser, with the purpose of improving the refrigeration cycle efficiency by further cooling the refrigerant at the condenser outlet, into the subcooled fluid region. The compressor was controlled through a simple on/off thermostat: it activated when the indoor temperature exceeded 25 °C and deactivated when the temperature dropped below 22 °C. The evaporated refrigerant flow rate was controlled by modulating the expansion valve orifice opening to consistently achieve the design evaporator super-heating. While evaporator super-heating remained constant, condenser subcooling varied dynamically depending on the heat rejected by the DRC panels. Greater radiative cooling flux enhanced subcooling, resulting in an improved Energy Efficiency Ratio (EER) and reduced compressor energy consumption. To ensure comparability across different scenarios, the analysis assumed the same cooling system design and refrigeration cycle for the VCRS in all tested locations.

2.2.2. Fan-coil units

The cooling effect generated at the VCRS evaporator was transferred to the conditioned space of the building through a FCU (modeled as a tube-fin heat exchanger). The FCU operated within a closed circuit that included a circulation pump and a small thermal fluid reservoir. The thermal fluid consisted of a mixture of 80 % water and 20 % ethylene glycol (EG). The circulation pump was activated simultaneously with the VCRS compressor, following an on/off control logic governed by the building thermostat.

2.2.3. Subcooler

A closed water-EG circuit coupled the DRC panels to the VCRS condenser. This loop included a circulation pump, a small tank, and a subcooler, i.e. the heat exchanger providing extra subcooling to the VCRS condenser. The subcooler was modeled as a tube-in-tube heat exchanger, with the water-EG mixture flowing on the shell side and R1234yf on the tube side. The subcooler size is a critical parameter for ensuring the proper operation of the DRC-based circuit. It was designed to deliver the additional cooling provided by the DRC panels, with its size determined based on the target temperature change of R1234yf across the subcooler (design subcooling $\Delta T_{D,sc}$). However, actual refrigerant subcooling (ΔT_{sc}) was typically lower than the design value in dynamic variation, due to the fluctuating atmospheric conditions. During the sensitivity analysis, the subcooler size was adjusted by varying the tube length to achieve the design subcooling, while maintaining other geometric parameters constant.

2.3. DRC panel

The array of DRC panels was modeled as a flat plate radiator comprising an aluminum plate with a copper serpentine beneath it. Each panel had an effective radiating surface of 1 m^2 and more panels were connected in series to form an array with the desired total surface. Similar panel geometries have been investigated in previous studies [36,52]. The DRC material was applied to the top of the plate, facing the sky. Due to its thin-film nature (thickness in the order of 100 μm), the physical presence of the material was negligible, and only its optical spectral selective properties were considered. The heat rejected by the condenser within the subcooler is transferred to the panel serpentine pipe by convection via the water-EG mixture. The fluid heats the serpentine pipe, which in turn conducts heat to the aluminum plate. The activation of the DRC panels was controlled by a circulation

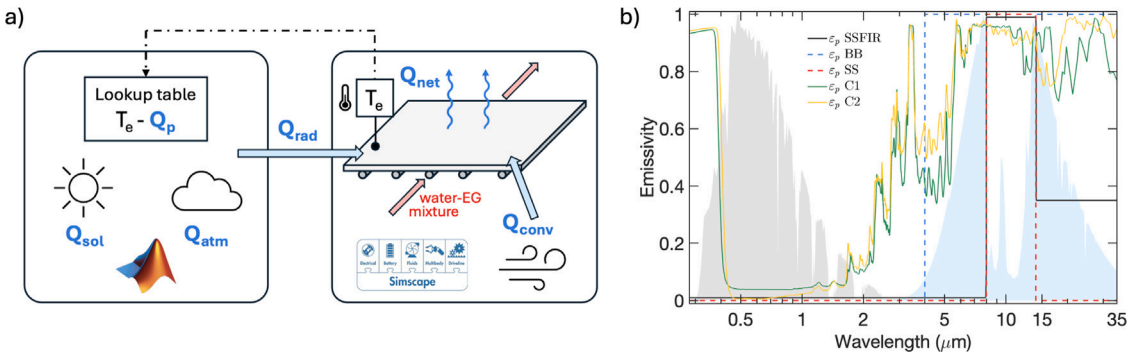

Fig. 2. (a) Schematic of the DRC panels model developed in *Simscape* environment with the entering/exiting fluxes. (b) Panel emissivity (ε_p) profiles of tested materials: Spectral Selective (SS), Broadband (BB), Spectral Selective with additional FIR emissivity (SSFIR), Commercial material 1 (C1) and Commercial material 2 (C2). The shaded gray is the normalized solar spectral radiance at 1.5 air mass [53]. The shaded blue area is the normalized atmospheric spectral radiance obtained through the model in Ref. [54] at 20 °C ambient temperature, 30 % relative humidity and clear sky. The atmospheric spectral radiance values applied in the model correspond to the specific time and location under investigation.

pump which ran exclusively when the VCRS was in operation. Consequently, the operational time of the DRC panels corresponds to the VCRS uptime.

At the emitter surface, the radiative cooling effect occurs. The net cooling power was determined by the interplay of radiative power from the panel (Q_p), absorbed solar power (Q_{sol}), absorbed atmospheric power (Q_{atm}) and the convective losses (Q_{conv}). As detailed in the following sections, the absorbed solar and atmospheric powers were precomputed over the entire temporal domain prior to starting the dynamic simulation. In contrast, the panel radiative power was evaluated using a one-dimensional lookup table that correlated the emitter temperature (T_e) with the corresponding panel radiative power. The total radiative power (Q_{rad}), comprising the absorbed solar power, the absorbed atmospheric power, and the emitted panel radiative power, was modeled in *Simscape* as a heat flow source directly applied to the emitter plate. Surface convective losses, conductive heat transfer between the emitter plate, and the serpentine and convective heat transfer within the serpentine were simulated in *Simscape* environment using conventional modeling blocks. A temperature sensor measured the emitter temperature and used it as the input signal to the lookup table. Fig. 2a illustrates a schematic representation of the DRC panels model.

2.3.1. Optical properties

The emitter spectral directional emissivity (ε_p) is a function of wavelength, angular direction, emitter temperature and surface azimuth angle. The limited temperature variation during operation makes the emissivity dependence on temperature negligible, and the dependence on azimuth is also insignificant for most engineering applications [22, 55]. Furthermore, for this purpose, a perfectly smooth, isotropic surface was considered, whose emissivity was assumed independent on the angular direction. For these reasons, the panel emissivity was considered as a function of wavelength only.

Fig. 2b shows the different emissivity profiles adopted in the simulations. An ideal spectrally-selective (SS) material has a unitary emissivity in the atmospheric window (8–13 μm) and zero emissivity elsewhere. A broadband (BB) emitter exhibits a black-body emissivity in the entire spectrum except that in the solar main spectral band and up to 4 μm. The SS emitter reaches the lowest equilibrium temperature but delivers minimal net cooling power when its surface temperature equals the ambient air temperature, conversely, the broadband emitter achieves the highest net cooling power but is the least effective at attaining significant sub-ambient temperatures [26]. Another interesting emissivity profile is that of a more realistic spectral selective emitter, featuring an exceptionally high emissivity of 99 % within the atmospheric window, 1 % in the solar spectrum range, and 35 % beyond 13 μm. This design minimizes heat absorption from thermal atmospheric flux while enabling the emitter to dissipate additional thermal energy in the far-infrared (FIR) spectrum; therefore, it is designated as SSFIR. Lastly, two emissivity profiles belonging to two real materials were tested (C1 and C2), both classifiable as real BB spectra. Material C1 is Spacecool Film Silver from *SpaceCool* company, while material C2 is a R&D developmental passive radiative cooling film provided by *3M* company [56].

2.3.2. Thermal balance

As previously mentioned, the fluxes acting on the DRC panels include the absorbed solar and atmospheric fluxes, the radiative flux emitted by the panel and convective losses. The following paragraphs provide the detailed equations adopted to estimate these components.

Panel radiative power

The radiative power emitted by the panel can be modeled as:

$$Q_p = A_p \pi \int_0^{\infty} \int_0^{\pi/2} \varepsilon_p(\lambda,\theta) I_b(\lambda, T_e) \sin(2\theta) \mathrm{d}\theta \, \mathrm{d}\lambda \quad (1)$$

where A_p is the total radiating surface area, I_b is the blackbody radiance and θ is the view-angle. This equation simplifies to

$$Q_p = A_p \pi \int_0^{\infty} \varepsilon_p(\lambda) I_b(\lambda, T_e) \mathrm{d}\lambda \quad (2)$$

considering that, due to the previous assumptions, the emissivity is a function only of wavelength. For the sake of simplicity, no obstacles or shadowing effects were considered in the panel emission hemisphere. The term $I_b(\lambda, T_e)$ is the blackbody spectral radiance at the emitter temperature T_e modeled with Planck's law:

$$I_b(\lambda, T) = \frac{2hc^2}{\lambda^5} \cdot \frac{1}{e^{hc/(\lambda k_B T)} - 1} \quad (3)$$

where $h = 6.6261\times10^{-34}$ J s is the Planck constant, $k_B = 1.3806\times10^{-23}$ J K^{-1} is the Boltzmann constant and $c = 2.9979\times10^{8}$ m s^{-1} is the speed of light in vacuum.

When dynamically simulated, Q_p is influenced only by variations in the emitter temperature over time, as the emissivity profile remains constant and does not vary over time. Consequently, prior to the simulation, a lookup table representing the panel flux was constructed. This involved solving Eq. (2) for a specified temperature range with application interest (from 0 °C to 40 °C) to encompass the potential operating temperatures of the emitter. This resulted in a lookup table correlating the emitter temperature with Q_p. The integral in Eq. (2) was numerically solved using the trapezoidal method over the wavelength range of 0 μm to 1000 μm. Beyond 1000 μm, the spectral radiation curve approaches zero, allowing this portion to be excluded from the calculation.

Solar absorbed power

The absorbed solar power was calculated using the following equation:

$$Q_{\mathrm{sol}} = A_{\mathrm{p}}\Psi \frac{\int_0^\infty \varepsilon_{\mathrm{p}}(\lambda) I_{\mathrm{AM1.5}}(\lambda)\,\mathrm{d}\lambda}{\int_0^\infty I_{\mathrm{AM1.5}}(\lambda)\,\mathrm{d}\lambda} = A_{\mathrm{p}}\Psi\alpha_{sol} \tag{4}$$

where $I_{\mathrm{AM1.5}}$ is the solar spectral radiance at an air mass (AM) of 1.5 (data from Ref. [53]) and Ψ is the solar irradiance at the ground. As the DRC panels were assumed to be oriented horizontally, no angular corrections for the angle of incidence were necessary. α_{sol} is the equivalent solar absorptivity of the DRC material in the solar spectrum band. By definition, the ideal SS and BB emitters exhibit zero emissivity in the solar region, resulting in an equivalent solar absorptivity of zero. Consequently, the solar component does not influence these materials. The SSFIR material is defined with a constant 1 % absorptivity in the solar spectrum, therefore its equivalent solar absorptivity is 1 %. The two commercial materials, however, feature complex emissivity profiles in the solar spectrum. The equivalent solar absorptivity was calculated as 9.54 % for material C1 and 8.89 % for material C2. The solar irradiance was obtained from the ERA5 database [47] for the specified location, based on the surface downward shortwave irradiance.

In Eq. (4), integrals were solved numerically using trapezoid method over the wavelength range of 0 μm to 4 μm. Assumed that the equivalent solar absorptivity remains constant over time, Eq. (4) can be solved prior to the dynamic simulations using the known irradiance signal. The resulting solution was then provided to the panel model as a time-dependent input signal.

Atmospheric absorbed power

The absorbed atmospheric power was modeled as:

$$Q_{\mathrm{atm}} = A_{\mathrm{p}} \int_0^\infty \varepsilon_{\mathrm{p}}(\lambda)\hat{q}_{\mathrm{atm}}(\lambda)\,\mathrm{d}\lambda \tag{5}$$

where $\hat{q}_{\mathrm{atm}}$ is the spectral hemispherical downward longwave atmospheric irradiance at the surface (DWLWAR) calculated over 16 spectral bands (from 3 μm to 1 mm), with an hourly time resolution, using the Longwave Rapid Radiative Transfer Model (RRTM_LW) [57,58]. RRTM_LW considers the effect of several atmospheric constituents. The distribution through the atmosphere of temperature, water vapor and ozone was sourced from ERA5 [47], while, for other species (CO_2, N_2O, CO, CH_4, O_2), seasonal latitude-dependent climatological values were employed. Finally, to account for the effect of cloud presence, profiles of cloud fraction, cloud ice water content and cloud liquid water content from ERA5 were used.

Also in this case, the integral in Eq. (5) was evaluated using the trapezoidal method over the wavelength dimension. The resulting equation was solved prior to the start of the dynamic simulations and supplied as a time-dependent signal.

Convection losses

The last term of the panel thermal balance is related to the convective losses, modeled as:

$$Q_{\mathrm{conv}} = A_{\mathrm{p}} h_{\mathrm{p}} (T_{\mathrm{amb}} - T_{\mathrm{e}}) \tag{6}$$

where T_{amb} is the ambient air temperature and h_{p} is the panel convective heat transfer coefficient. The panel was assumed perfectly insulated on its bottom and four lateral surfaces, leaving only the sky-facing surface A_{p} exposed to wind convection. The value of the convective heat transfer coefficient was modeled using the correlation [59]:

$$h_p = 8.3 + 2.5\frac{v_{\mathrm{w}}}{v_0} \tag{7}$$

where v_{w} is the wind velocity and $v_0 = 1\,\mathrm{m\,s^{-1}}$. Data for ambient temperature (air temperature measured at a height of 2 m above ground level) and wind velocity were sourced from the ERA5 database.

2.3.3. Geometry

The panel serpentine was sized in order to avoid pressure drops higher than 10 % the nominal working pressure value. The geometry and thermophysical data for a single DRC panel are reported in the Supplementary Material, Section S3. The thermal masses of the emitter and the serpentine correspond, respectively, to the thermal capacity of an aluminum plate and a copper pipe with the specified geometry. The panel was modeled using a lumped-parameter approach, trying to simplify its geometry to achieve good computational performance. Consequently, the system was characterized by only two temperatures: the emitter temperature, which served as the feedback signal for the lookup table, and the external pipe temperature. The thermal fluid flowing through the panels was pumped at an inlet pressure of 1.2 bar.

3. Results

3.1. Transients analysis

The implemented model was used to simulate the transient behavior of the entire system (building, FCU, VCRS, subcooler, and DRC panels) over a 92-day cooling period (June–August 2023). To simplify analysis and interpretation, integral parameters were used to capture the results of the transient dynamics. However, to illustrate the model potentialities and highlight notable dynamics, the transients for Las Vegas location for June 9th and 10th, for a system featuring 10 $\mathrm{m^2}$ of radiative panels coated with SSFIR material, are presented in Fig. 3.

Fig. 3a illustrates the variations in ambient temperature (T_{amb}), building temperature (T_{b}) and emitter temperature (T_{e}) over the two-day period. The building temperature oscillated between upper and lower thermostat set points of 25 °C and 22 °C, respectively. The emitter temperature consistently remained below the ambient temperature, demonstrating the efficacy of the spectral selective material in maintaining sub-ambient panel temperatures. The average subcooling achieved across the two days was 4.8 °C. Fig. 3b depicts the various fluxes acting on the radiative panel. The solar radiation absorbed by the panel was modest due to the low absorptivity (1 %) of the SSFIR material within the solar spectrum. Conversely, the atmospheric flux was significant because the atmosphere radiates energy in the same spectral range where the panel exhibits high emissivity and absorptivity. The convective heat losses fluctuated in alignment with the panel subcooling trend. Throughout the analyzed period, the convective flux remained positive, indicating that the panel was heated by the surrounding air, as the emitter temperature was consistently below the ambient temperature. The radiative flux from the panel mirrored the emitter temperature general trend.

The net power Q_{net} represents the heat rejected by the thermal fluid circulating through the serpentine system, corresponding to the useful cooling effect provided by the radiative panel. Considering the thermal balance on the DRC material surface:

$$Q_{\mathrm{net}} = Q_{\mathrm{p}} - Q_{\mathrm{atm}} - Q_{\mathrm{sol}} \mp Q_{\mathrm{conv}} + mc_{\mathrm{p}}\frac{\mathrm{d}T}{\mathrm{d}t} \tag{8}$$

where $mc_{\mathrm{p}}\frac{\mathrm{d}T}{\mathrm{d}t}$ is the heat accumulation term. The Q_{net} profile is complex, as it is influenced by the interplay between the radiative panels and the VCRS. Low duration peaks in the net flux occur upon activation of the panel circulation pump. These spikes arise because, during VCRS idling, the thermal fluid within the pipes cools down due to the absence of heat input from the subcooler. Upon restarting the circulation pump, the substantial temperature differential between the fluid and the subcooler results in transient spikes in thermal flux exchange. However, these spikes are short-lived, lasting only a few minutes (1–10 min) and depend on the panels thermal mass.

Fig. 3c presents the subcooling of the VCRS refrigerant fluid during operation, showing zero subcooling when the system is idle. Fig. 3d provides an overview of refrigerant subcooling throughout the entire time domain. When considering only periods of VCRS operation, an average refrigerant subcooling of 7.7 °C was observed.

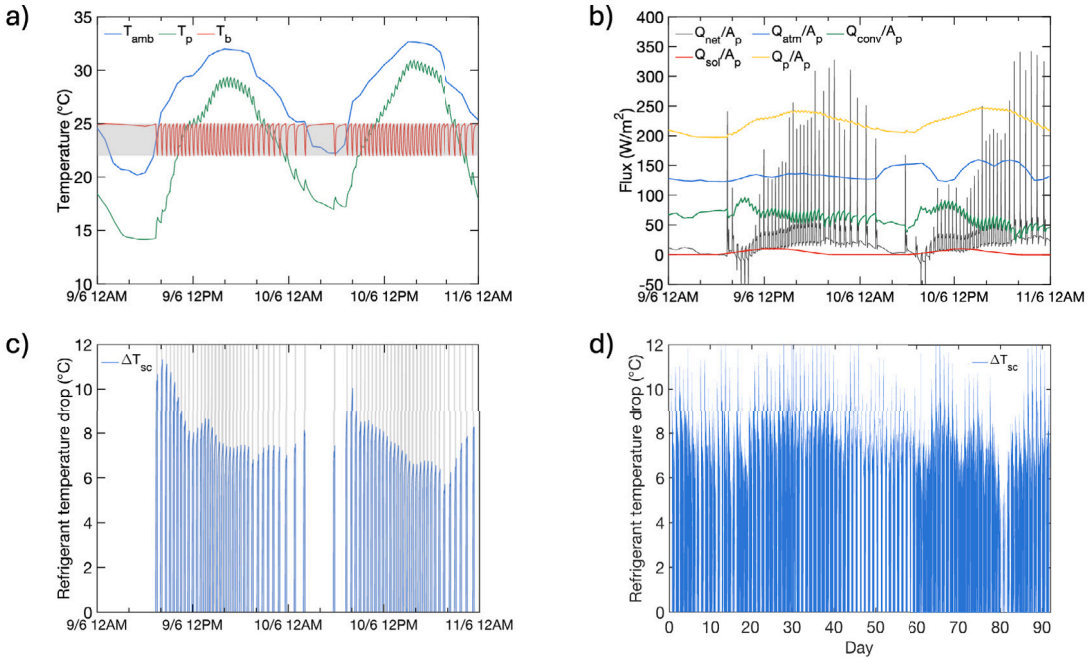

Fig. 3. Model transient results across June 9th and 10th 2023: (a) ambient, building and emitter temperature (the shaded gray area indicates the indoor temperature target range); (b) atmospheric absorbed flux, solar absorbed flux, panel radiative flux, convective flux and net flux; (c) refrigerant fluid subcooling (the shaded gray area represents the VCRS uptime). Model transient results across June, July and August 2023: (d) refrigerant fluid subcooling. These results are for a DRC-system located in Las Vegas with 10 m^2 of radiative surface, 1.5 $L\,min^{-1}\,m^{-2}$ of panel thermal fluid flow rate and 12 °C design subcooling; the cooling load is for the *Standard building*.

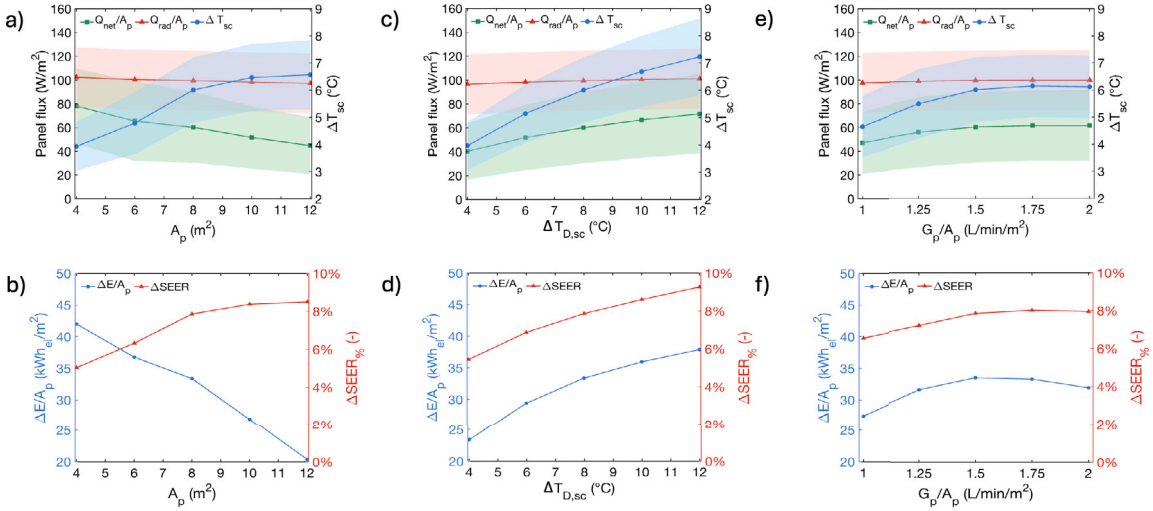

Fig. 4. Sensitivity analysis on panel net and radiative flux, subcooler temperature drop, specific electric energy savings and seasonal EER variation. (a–b) The effect of panel array surface at $G_p/A_p = 1.5\,L\,min^{-1}\,m^{-2}$ and $\Delta T_{D,sc} = 8\,°C$. (c–d) The effect of subcooler size at $G_p/A_p = 1.5\,L\,min^{-1}\,m^{-2}$ and $A_p = 8\,m^2$. (e–f) The effect of panel specific flow rate at $\Delta T_{D,sc} = 8\,°C$ and $A_p = 8\,m^2$. These results are for a DRC system located in Las Vegas simulated with meteorological data of June-August; the cooling load is for the *Standard building*.

3.2. Parametric analysis

A parametric analysis of key operational variables in the plant was then performed. A dynamic simulation was conducted over the entire time domain, during which the temporal evolution of the selected variables was recorded. Subsequently, the resulting signals were post-processed to derive their mean values and associated variability. The mean value was calculated as the integral average of the signal, while the variability was quantified as the standard deviation of the mean. The standard deviation was chosen to represent variability because alternative metrics, such as minimum and maximum values, would be less informative due to the influence of transient spikes and short-duration local fluctuations.

Three parameters were varied during the parametric analysis: the panel array radiative surface (A_p), the subcooler size, represented as the design refrigerant subcooling ($\Delta T_{D,sc}$), and the panel HTF flow rate per unit surface (G_p/A_p). Their impact was evaluated by monitoring key quantities, specifically the net power (Q_{net}), refrigerant subcooling

(ΔT_{sc}), radiative power (Q_{rad}), electric energy savings (ΔE), and the seasonal EER variation ($\Delta SEER_{\%}$).

The radiative power, defined as

$$Q_{rad} = Q_p - Q_{atm} - Q_{sol} \tag{9}$$

quantifies the radiative power dissipated by the panel, excluding contributions from other heat transfer mechanisms.

The electric energy savings are expressed as

$$\Delta E = E^0 - E \tag{10}$$

where E is the total system electricity consumption, and E^0 corresponds to the consumption in the absence of DRC panels and the additional subcooler. Two simulations, with and without radiative cooling, are conducted to compute this parameter. The total electricity consumption is defined as

$$E = E_{cmp} + E_{fan,b} + E_{fan,c} + E_{pmp,b} + E_{pmp,p} \tag{11}$$

comprising the energy consumed by the compressor (E_{cmp}), FCU fans ($E_{fan,b}$), air-cooled condenser fan ($E_{fan,c}$), FCU circulation pump ($E_{pmp,b}$), and radiative panel circuit circulation pump ($E_{pmp,p}$). For the non-radiative cooling scenario, electricity consumption is

$$E^0 = E^0_{cmp} + E^0_{fan,b} + E^0_{fan,c} + E^0_{pmp,b} \tag{12}$$

as the panel circuit circulation pump is absent. The energy savings generated by the DRC panels result from reduced VCRS usage, as enhanced subcooling provided by the DRC panels increases the refrigerant cycle area and EER, leading to decreased compressor runtime.

The seasonal EER (SEER) [60] is given by

$$SEER = \frac{E_{evap}}{E_{cmp}} \tag{13}$$

where E_{evap} is the thermal energy absorbed at the VCRS evaporator. Analogously, for the scenario without radiative cooling, SEER is defined as $SEER^0 = E^0_{evap}/E^0_{cmp}$. The relative SEER improvement is then

$$\Delta SEER_{\%} = \frac{SEER - SEER^0}{SEER^0}. \tag{14}$$

Fig. 4 presents the results of the parametric analysis conducted under Las Vegas climate for the *Standard building* typology. Figs. 4a and 4b illustrate the influence of panel surface area on the key parameters. Predictably, the average refrigerant subcooling increases with the panel area until saturation is reached. The limiting factor is the fixed size of the subcooler, which cannot deliver more than the design subcooling to the refrigerant. The specific energy savings diminish as the panel area increases. This phenomenon occurs because smaller panel surfaces, at parity of heat transfer from the subcooler to the radiative circuit, achieve higher temperatures compared to larger panel areas. Given that radiative power scales with the fourth power of temperature, higher surface temperatures result in more efficient energy rejection and, consequently, higher specific energy savings. The average radiative flux follows a similar trend for the same reason. The net average flux, however, remains unaffected by variations in panel surface area, as the rejectable energy is determined by the fixed size of the heat exchanger. The SEER increase closely mirrors the trend of average refrigerant subcooling.

Figs. 4c and 4d show the impact of subcooler size. Average refrigerant subcooling, seasonal EER variation, average net flux, and specific electricity savings all increase monotonically with design subcooling until saturation. The specific thermal energy rejected by the panels exhibits the same trend as specific electricity savings. At the maximum design subcooling evaluated (12 °C), the SEER increased by 9.4 % and electricity consumption decreased by 8.4 %. While higher design subcooling could be achieved, such increases would be inconsistent with the concept of retrofitting a conventional VCRS designed for operation within a specific refrigerant cycle.

Figs. 4e and 4f report the effects of the panel specific flow rate. The trend indicates that changes in flow rate have a minimal effect on energy savings. In the tested setup, the highest energy savings occur at $1.5\,L\,min^{-1}\,m^{-2}$. Moreover, as flow rates increase, pressure drops within the panel circuit also rise, leading to higher energy consumption by the circulation pump. This results in a slight decrease in total energy savings beyond $1.5\,L\,min^{-1}\,m^{-2}$.

3.3. Effect of geographical location

Several atmospheric parameters, such as humidity and cloud cover can significantly influence the performance of radiative coolers [9]. The presence of clouds, in particular, plays a critical role. While clouds reduce the amount of absorbed solar radiation, they also degrade the effectiveness of DRC systems, since they reduce atmospheric transmissivity in the 8–13 μm window and increase the amount of infrared radiation reaching the surface. The latter point is highlighted in Fig. 5, where the results of the radiative transfer simulations carried out with RRTM_LW (panel a) are shown, together with the main atmospheric parameters (panel b). In particular, the time evolution of DWLWAR is shown spectrally integrated over the whole infrared as well as limited to the spectral range of the atmospheric window. While the total radiation is strongly influenced by the temperature of the lower layers of the atmosphere, the irradiance in the atmospheric window is modulated by clouds: the absence of clouds is associated to a decrease in the radiation values. By contrast, lower and thicker clouds cause an increase of DWLWAR since their effect is equivalent to that of a gray-body emitting at the temperature of the cloud altitude. While Fig. 5 refers to Las Vegas, the same behavior is observed in the other simulated locations (Supplementary Material, Figures S8-S10). More broadly, the total column water vapor in the atmosphere limits the cooling potential [61]. Consequently, DRC systems have shown to be highly efficient in hot and arid environments, often desert-like regions, such as the American Southwest and the Arabian Peninsula [28,36,44,62].

The DRC system was tested in 4 different cities: Las Vegas, Riyadh, Madrid and Turin. Las Vegas and Riyadh, according to Köppen-Geiger (KG) classification [63], have a hot desert climate characterized by extremely low annual precipitation and high temperatures, particularly in summer. Madrid has a hot-summer Mediterranean climate, characterized by dry summers, while Turin has a warm temperate oceanic climate with warm summers and rainfall distributed throughout the year. Table 1 presents the mean values of key atmospheric variables during the simulated period for the four locations.

Fig. 6a shows the electric energy savings resulting from the application of a DRC-driven subcooler to the same VCRS under different geographical locations and for two distinct energy classes of buildings. The operational parameters were held constant across all locations. Among the evaluated sites, Riyadh, characterized by the highest average ambient temperature, achieved the greatest seasonal electric energy savings: $368.6\,kW\,h_{el}$ ($46.1\,kW\,h_{el}\,m^{-2}_{DRC}$) for the *Standard building* and $303.9\,kW\,h_{el}$ ($38.0\,kW\,h_{el}\,m^{-2}_{DRC}$) for the *Modern building*. It is followed by Las Vegas (37.5 and $27.7\,kW\,h_{el}\,m^{-2}_{DRC}$), Madrid ($20.1\,kW\,h_{el}\,m^{-2}_{DRC}$ and $12.5\,kW\,h_{el}\,m^{-2}_{DRC}$), and Turin ($9.6\,kW\,h_{el}\,m^{-2}_{DRC}$ and $7.5\,kW\,h_{el}\,m^{-2}_{DRC}$) for *Standard* and *Modern* buildings, respectively. Riyadh showed the greatest absolute energy savings due to the high cooling demand of the building and the most favorable atmospheric conditions for radiative cooling among the locations tested, featuring the lowest average humidity and cloud cover. On the other hand, Turin achieved the lowest energy savings because of a lower cooling load requirement and less favorable climatic conditions, characterized by significant cloud cover and higher relative humidity during the summer months. For all four locations, the building with lower thermal insulation (*Standard building*) achieved greater absolute energy savings compared to the modern building. This is explained by the higher operational runtime of the VCRS, which extends the duration over which the benefits of radiative cooling are applied. However, locations yielding

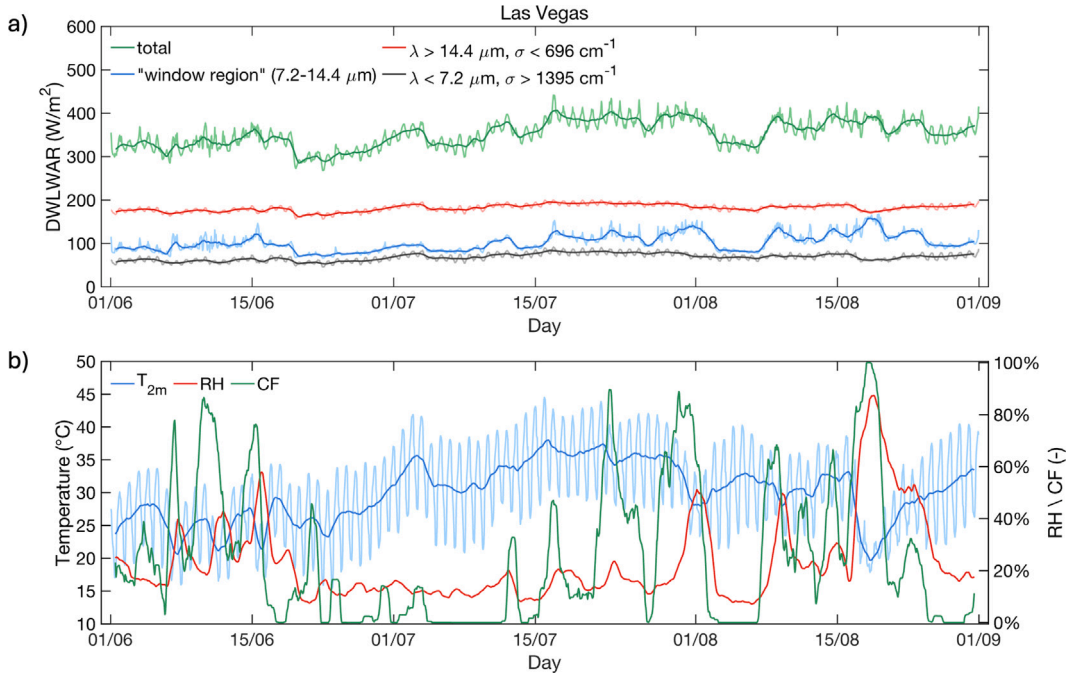

Fig. 5. (a) Time series of the downwelling atmospheric irradiance for Las Vegas. For each quantity, the lighter curves are at hourly resolution, the darker ones are obtained applying a 24-h moving average to suppress the daily cycle. The green curves are for the total spectral interval (3 μm – 1 mm) while the blue curves are for the atmospheric window interval. The red and black curves are for wavelengths above and below the atmospheric window, respectively. (b) Time series for a selection of atmospheric parameters. The light blue curve is for air temperature at 2 m above ground with hourly resolution. The other curves are obtained applying a 24-h moving average to suppress the daily cycle: air-temperature at 2 m above ground (blue, T_{2m}), relative humidity (red, RH) and cloud cover (green, CF).

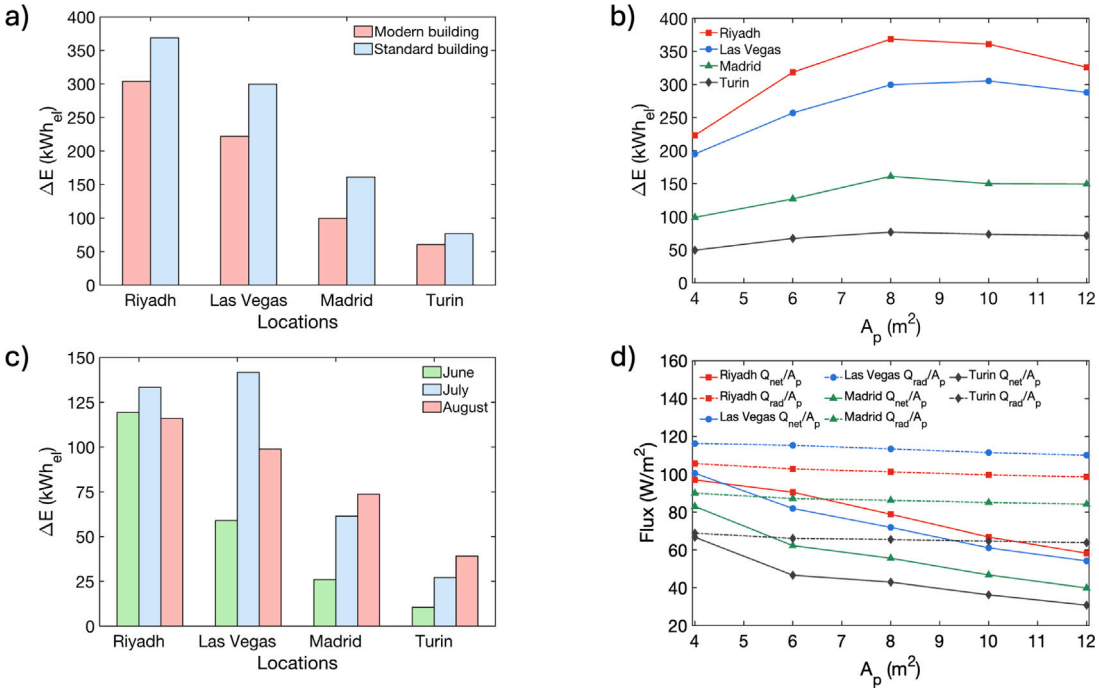

Fig. 6. Analysis of DRC performance by geographical location. (a) Electric energy savings at $A_p = 8\,m^2$, $G_p/A_p = 1.5\,L\,min^{-1}\,m^{-2}$ and $\Delta T_{D,sc} = 12\,°C$ for *Modern* and *Standard building*. (b) The effect of panel surface area on electric energy savings at $G_p/A_p = 1.5\,L\,min^{-1}\,m^{-2}$ and $\Delta T_{D,sc} = 12\,°C$ for the *Standard building*. (c) Electric energy savings at $A_p = 8\,m^2$, $G_p/A_p = 1.5\,L\,min^{-1}\,m^{-2}$ and $\Delta T_{D,sc} = 12\,°C$ for the *Standard building* across June-August. (d) The effect of panel surface area on average net and radiative flux at $G_p/A_p = 1.5\,L\,min^{-1}\,m^{-2}$ and $\Delta T_{D,sc} = 12\,°C$ for the *Standard building*.

the highest absolute energy savings did not necessarily correspond to those achieving the highest relative energy reductions compared to the baseline scenario. Specifically, Riyadh, Las Vegas, Madrid, and Turin yielded relative energy reductions of −6.3 %, −8.1 %, −9.9 % and −6.9 %, respectively, for the *Standard building* scenario, and −8.0 %, −9.0 %, −9.0 % and −7.8 %, respectively, for the *New building* scenario. Notably, Madrid achieved the highest relative energy reduction. These findings suggest that the relative electric energy reduction, often employed in the literature as a performance metric for radiative cooling, may not adequately capture the impact of this technology. Instead, the absolute energy savings, also normalized by the unit area of radiative cooling material or conditioned building area, provide a more representative measure of performance.

Fig. 6b depicts the relationship between electric energy savings and the panel array surface area across the four locations. Energy savings increase with panel size until reaching a peak, after which they slightly decrease, indicating that the thermal energy rejected by the panels has reached saturation. Increasing the surface area further raises pumping energy demand, which reduces net savings. The optimal DRC panel size depends heavily on operational factors such as subcooler size, HTF flow rate, and local atmospheric conditions. Generally, it is advisable to select the largest subcooler compatible with the retrofit and then adjust the DRC panel surface area to maximize energy savings without incurring excessive pumping losses. This sizing process should be based on representative atmospheric data or Typical Meteorological Year (TMY) information.

Fig. 6c shows the distribution of energy savings across the three simulated months. In Riyadh, the energy savings remained nearly constant throughout the period, whereas Las Vegas exhibited a significant peak in July. In Turin and Madrid, August and July were the hottest months, corresponding to the highest cooling demand. This highlights that the absolute energy savings of DRC-enhanced VCRS systems are predominantly influenced by the VCRS runtime, or building cooling demand, with meteorological conditions exerting a secondary effect, primarily impacting radiative cooler performance. This finding aligns with conclusions reported in Ref. [37]. It is important to note that the energy savings presented here do not reflect the general performance of the technology across the simulated locations, as 2023 meteorological data were employed. For broader applicability, TMY data should be used [64]. Additionally, locations such as Las Vegas and Riyadh exhibit significant cooling demand in months like May and September, which were not included in the simulation. The primary aim of using specific meteorological data was to evaluate system performance under diverse meteorological conditions and varying cooling demands, while also capturing localized effects that TMY data may fail to represent [65].

Fig. 6d shows the variation in panel net and radiative flux as a function of panel area for the four locations. The analysis of this plot is essential for establishing whether the DRC emitters are predominantly operating below or above ambient temperature, noting that a configuration operating mainly below ambient may still experience rare transient periods above ambient. When operating above ambient temperature, the net flux exceeds the radiative flux due to the favorable effect of convection. Such a condition may occur if the DRC units are undersized and unable to reject sufficient heat to sustain sub-ambient operation. This behavior can be further verified by the average emitter temperature during VCRS operation, which, in such cases, would exceed the average ambient temperature. Although this was not observed under the tested locations and operating parameters, it should be explicitly accounted for in the system sizing process. Operating above ambient temperature is not inherently disadvantageous, as the radiative flux of the panel increases with temperature. However, in the setup analyzed in this work, the DRC panel array serves as an extension of the condenser. Therefore, maintaining the DRC circuit fluid below ambient temperature facilitates additional subcooling of the refrigerant when it exits the air-cooled condenser at temperatures near ambient.

Table 1
Geographical and meteorological data for the four locations under analysis. Air temperature, relative humidity, total cloud cover, DWLWAR and wind velocity are reported as averages over the simulation period. These data were obtained from the ERA5 database [47].

	Riyadh	Las Vegas	Madrid	Turin
Latitude	24.7	36.2	40.4	45.0
Longitude	46.7	−115.1	−3.7	7.7
KG zone	BWh	BWh	Csa	Cfa
Air temperature (°C)	36.7	29.2	26.4	23.7
Relative humidity (%)	11.4	23.7	39.1	58.6
Total cloud cover (%)	13.1	25.9	25.0	46.2
DWLWAR ($W\,m^{-2}$)	384	357	355	362
Wind velocity ($m\,s^{-1}$)	3.0	2.4	2.5	2.1

3.4. Effect of emitter material

Fig. 7a shows the electric energy savings for Las Vegas across the five emissivity profiles discussed in Section 2.3.1. The BB emitter achieved the highest energy reduction (−8.5 %), followed by the SS (−8.3 %), SSFIR (−8.2 %), and the commercial materials C2 (−7.2 %) and C1 (−7.0 %). These findings yield two key insights. (i) The spectral selective emitter with expanded emissivity (SSFIR) in the infrared band (35 %) exhibited performance closely approaching that of the ideal spectral selective emitter (SS) with zero emissivity outside the atmospheric window, while remaining slightly inferior to the broadband (BB) emitter. These results indicate that, for applications involving a DRC-enhanced VCRS, materials with highly tuned emissivity profiles matching the atmospheric window may not be necessary. Instead, materials with broadband infrared emissivity could provide a simpler and more effective solution. A moderate emissivity above 13 μm may enhance energy rejection to the sky, despite increased absorption of DWLWAR. This observation is consistent with prior studies demonstrating that selective materials optimized for the second atmospheric window (16–25 μm) can outperform single-band selective emitters, particularly in arid climates [66]. (ii) Both commercial materials, which exhibit broadband emissivity profiles, performed comparably to the ideal broadband emitter.

Fig. 7b presents the net and radiative average fluxes, along with their variability (expressed as standard deviation), for the different materials. These flux trends align with the energy savings trends. Notably, the radiative flux variability bars provide additional insights. The SS emitter showed the narrowest variability because it is immune to solar flux variability and poorly affected by atmospheric fluxes fluctuations. In contrast, the BB emitter showed higher variability, consistent with its higher sensitivity to DWLWAR. Furthermore, as confirmed by literature [9,26], BB emitter achieved the highest radiative flux among ideal emitters. For commercial materials (C1 and C2), radiative flux variability was even more pronounced, mirroring the behavior of the ideal BB. Owing to this increased variability, the commercial materials were more susceptible to transient above-ambient conditions during operation, thereby benefiting from convective contributions.

The characteristic curve of DRC emitters is presented in Fig. 8, depicting the net cooling effect as a function of the temperature difference between the environment and the emitter. This curve was obtained by applying linear regression on the operational data points observed during simulations. Post-processing was performed to exclude the working points during transient operation, such as net flux spikes observed during VCRS startup. More details about the post-processing methodology are provided in Supplementary Material, Section S4. Working points are significantly scattered in the flux-temperature difference plane due to variability in atmospheric conditions, including irradiance, relative humidity, wind velocity, and cloud cover. Nevertheless, these data are well-approximated by linear regression for the SS, BB and SSFIR emitters, whereas data for commercial materials show slightly higher variability. At zero subcooling, the BB emitter achieves the highest

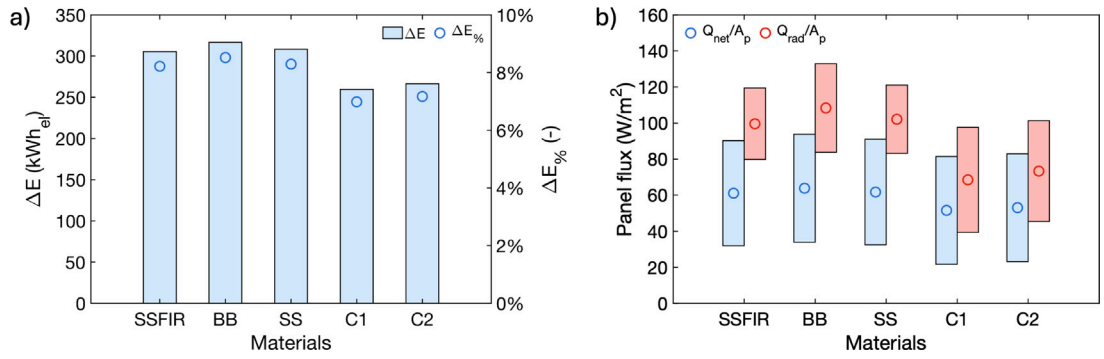

Fig. 7. Effect of 5 different DRC emissivity profiles (SSFIR, BB, SS, C1 and C2) on: (a) Electric absolute (bars) and relative (markers) energy savings; (b) Radiative and net fluxes (markers indicate mean values, while bars represent variability). These results are for a DRC system with $A_p = 10\,m^2$, $G_p/A_p = 1.5\,L\,min^{-1}\,m^{-2}$, $\Delta T_{D,sc} = 12\,°C$, located in Las Vegas and simulated with meteorological data of June-August; the cooling load is for the *Standard building*.

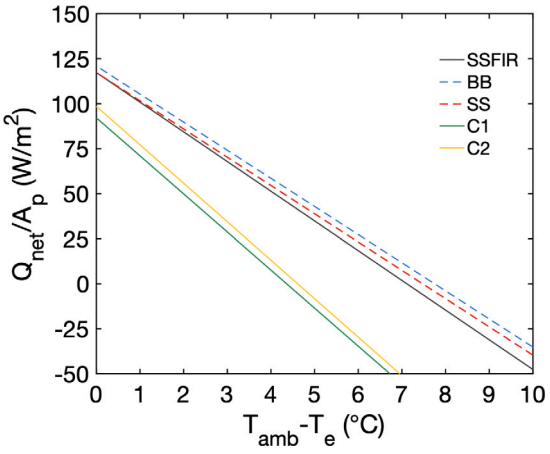

Fig. 8. DRC panel net flux versus ambient-emitter temperature difference curve for SSFIR, BB, SS, C1 and C2 materials. These results are for a DRC system with $A_p = 10\,m^2$, $G_p/A_p = 1.5\,L\,min^{-1}\,m^{-2}$, $\Delta T_{D,sc} = 12\,°C$, located in Las Vegas and simulated with meteorological data of June–August; the cooling load is for the *Standard building*.

net flux, followed by the SS, the SSFIR and the commercial materials. Under the operational conditions explored, the broadband material outperforms the others, as previously confirmed by the energy savings analysis (Fig. 7a).

It is important to emphasize that the characteristics presented in Fig. 8 do not correspond to any specific operating conditions of the DRC system. Instead, they represent averaged characteristics that synthesize the behavior of different DRC emitters under the range of meteorological conditions observed over the entire cooling season. These conditions include nighttime and high-irradiance periods, clear-sky and overcast conditions, as well as varying ranges of temperature, relative humidity, and wind velocity. For these reasons, such curves are useful for rapid comparison among different emitters and can assist technicians in selecting materials according to the target design conditions to be achieved in the plant.

4. Discussion

4.1. Model validation

The model presented in this study provides a comprehensive overview of the main design parameters that affect the performance of DRC-enhanced VCRS systems. Due to the novelty of the technology analyzed, only a limited number of studies investigating VCRS systems with a DRC-driven subcooler are currently available in the literature [36,37,41,67]. These studies vary substantially in terms of modeling assumptions, simulation tools, and system configurations, making them unsuitable for direct validation of the proposed model. For this reason, a component-wise validation approach was adopted. For the conventional components, namely the VCRS and the FCUs, a simplified validation was sufficient. Each device was first sized according to the thermal demand of the building under design conditions. The components were then modeled in the *Simscape* environment and tested individually by applying the steady-state design boundary conditions. The simulations confirmed that the system outputs – such as temperatures, pressures, and qualities – converged to the expected design targets, indicating correct sizing and functionality. For the novel component, the DRC panels, a more detailed experimental validation was carried out. Specifically, the model developed to simulate the dynamic behavior of the DRC material was validated against experimental data from a facility described in a previously published study [68], which tested a commercial DRC material under real outdoor conditions. The validation process, detailed in the Supplementary Material, Section S5, resulted in a mean absolute error below 5 % across five days, including both clear and cloudy sky conditions, thereby supporting the reliability of the DRC model.

4.2. Effect of VCRS size and runtime

During the parametric analysis, a DRC-enhanced VCRS was tested in Las Vegas climate using $8\,m^2$ of SSFIR radiative surface, with the additional subcooler sized to achieve varying levels of subcooling. A design subcooling of 8 °C (+9.1 % increase in condenser cooling capacity) resulted in a 7.2% reduction in energy consumption during the cooling season. However, the actual refrigerant subcooling achieved was $(6.0 \pm 1.2)\,°C$, as the DRC panels did not operate consistently under design conditions. Increasing the subcooler and DRC panel size enhances energy savings. For example, the same system designed for 14 °C of refrigerant subcooling (+15.7 % condenser capacity) with $16\,m^2$ (two parallel rows of $8\,m^2$ each) of radiative surface yielded a 9.6 % reduction in energy consumption and achieved $(9.6 \pm 1.8)\,°C$ of additional subcooling. Using a BB emitter in the same configuration produced a 10.1 % reduction in energy use. Consequently, the relative impact on energy savings is highly dependent on both the DRC panel area and the subcooler size. The VCRS size and, in particular, the design condensation temperature have a substantial impact on system performance. The closer the condensation temperature is to the ambient temperature, the greater the benefits of additional subcooling.

The absolute energy savings achieved by DRC-assisted VCRSs appear to be predominantly influenced by the VCRS runtime, with climate types and meteorological conditions playing a secondary role. Therefore, for a given DRC device, energy savings increase as the VCRS

uptime rises. This principle is corroborated by previous studies [37] and is further discussed in Supplementary Material, Fig. S5.

Goldstein et al. [36] demonstrated a 21 % reduction in energy consumption in Las Vegas climate using a DRC-assisted VCRS applied to a large office building, where an array of DRC panels covered 60 % of roof area. This study highlights the greater effectiveness of DRC systems at larger scales and in buildings with a high roof surface-to-volume ratio, as such configurations require extensive roof surfaces. Conversely, in the present analysis, a two-story single-family building with an additional third story consisting of an unconditioned attic was considered, using only a small portion of the roof area (for a $8\,m^2$ radiative surface only 8.3 % of roof surface was exploited). In multistory buildings, the roof surface-to-volume ratio is low, limiting the heat rejection capacity of the DRC panels relative to the total cooling load. In conclusion, the performance and impact on energy savings of DRC-assisted VCRSs are influenced not only by operational and design parameters, such as radiative area, subcooler size, and VCRS capacity, but also by the cooling load of the building and VCRS runtime.

Another aspect that should be properly addressed during the sizing of DRC-enhanced cooling systems is their economic viability. The configuration that maximizes energy savings may not necessarily maximize profitability or minimize the payback time of the plant. For instance, as shown in Section 3.2, increasing the size of the DRC-driven subcooler enhances energy savings and thus increases potential revenues. However, this also raises capital costs, highlighting the existence of an optimal subcooler size. These trade-offs call for a comprehensive techno-economic analysis. Due to the current limitations of DRC technologies – including their limited market availability and the absence of reliable cost functions – a detailed economic assessment may be premature. Some insights into the economics of DRC systems can be found in Ref. [37], while related analyses for different DRC technologies have been reported by Zhang et al. [41] and Yadav et al. [69].

4.3. Effect of material aging

An underexplored topic in the literature of DRC materials is the impact of natural environmental aging and surface soiling, processes that can progressively degrade radiative cooling performance. Natural aging occurs primarily through three mechanisms: ultraviolet (UV) radiation exposure, thermal aging, and chemical degradation. Among these, UV exposure exerts the most significant effect, diminishing ultra-white appearance of DRC materials or, more broadly, their solar reflectivity [70] (while the influence on infrared emissivity, and hence nighttime cooling potential, is usually negligible [71]). A sensitivity analysis was conducted to quantify the influence of UV-induced degradation on system performance. Results (Supplementary Material, Fig. S6) indicate that a 3 % reduction in solar reflectivity leads to a 6.3 % decline in energy savings relative to the baseline, while a 10 % reflectivity loss results in a 17.2 % reduction.

The effects of surface soiling are more challenging to model and remain insufficiently addressed in current research. A study by Fan et al. [72] reported that, at low dust levels, cooling power decreases by approximately $7.1\,W\,m^{-2}$ for every $0.1\,mg\,cm^{-2}$ increase of dust mass, with complete loss of cooling capability at medium and high dust loads, underlining the importance of keeping DRC surfaces clean.

5. Conclusion

DRC technologies have the potential to enhance the sustainability and energy efficiency of residential buildings through their integration with conventional thermal management systems. This study arises from the need to characterize the operation and identify the primary parameters influencing the performance of a DRC-enhanced VCRSs, an area that remains quite unexplored in the scientific literature. To address this gap, a dynamic model of a residential building with the innovative thermal management system was developed. The transient behavior of the system was simulated over the cooling season June–August 2023, using hourly meteorological data at four distinct locations: Las Vegas, Riyadh, Madrid, and Turin. This simulations included the calculation of the spectrally-resolved effects of atmospheric radiation and, notably, the significant effect of clouds was also simulated.

The highly fluctuating trends of key variables, such as refrigerant subcooling, emitter temperature, and panel net flux, were analyzed. A parametric analysis revealed that electric energy savings steadily increase as the subcooler size grows. Electric energy savings also increase with panel array size, but eventually the additional energy consumption of the circulation pump outweighs the benefits of adding more panels, causing a slight decline. In contrast, the thermal fluid flow rate through the panels has minimal impact on the overall results. The system performance was subsequently assessed across four locations, revealing significant energy savings in hot and arid climates such as Las Vegas ($37.5\,kW\,h_{el}\,m_{DRC}^{-2}$) and Riyadh ($46.1\,kW\,h_{el}\,m_{DRC}^{-2}$), while moderate savings were observed in temperate climates like Madrid ($20.1\,kW\,h_{el}\,m_{DRC}^{-2}$) and Turin ($9.6\,kW\,h_{el}\,m_{DRC}^{-2}$). Notably, the locations with the highest absolute energy savings did not coincide with those achieving the highest relative energy savings compared to scenarios without radiative cooling panels. The influence of different DRC emitters was also investigated: the ideal broadband material slightly outperformed the spectral selective option, while the two commercial broadband materials tested exhibited moderately lower performance compared to the ideal broadband.

Given the current lack of experimental measurements on DRC-enhanced VCRS and the absence of a standardized methodology for characterizing DRC materials [73], numerical simulations, such as those presented in this study, are a valuable tool for assessing the impact of DRC technologies on AC systems. However, future researches testing full-scale setups are necessary to refine and consolidate these findings. Further studies should also focus on developing advanced control strategies to optimize the performance of DRC active systems. Since the benefits of DRC-enhanced VCRS increase with extended operation, new research should explore the applicability of this technology in high-thermal-load facilities with continuous cooling demands, such as data centers and refrigerated warehouses. Additionally, economic analyses are needed to assess the long-term profitability of DRC systems, alongside studies on the effects of natural aging and soiling to better understand their durability and performance over time.

Radiative cooling panels for residential applications face competition from other rooftop technologies, such as solar thermal and photovoltaic panels, due to limited roof space. Consequently, DRC technology may be more suitable for buildings with a high roof area-to-volume ratio, such as pavilions and warehouses, and in partially shaded areas of the roof, where they benefit from the effects of shadowing. A promising approach to address this competition involves integrating radiative cooling with other rooftop technologies to enable year-round utilization, and future research should focus on developing such solutions to maximize the adoption and efficiency of DRC technologies.

CRediT authorship contribution statement

Davide Forte: Writing – original draft, Visualization, Software, Methodology, Investigation, Formal analysis, Data curation. **Claudio Belotti:** Writing – original draft, Visualization, Methodology, Investigation, Funding acquisition, Data curation. **Lorenzo Pattelli:** Writing – review & editing, Validation, Supervision, Methodology, Funding acquisition. **Matteo Morciano:** Writing – review & editing, Validation, Methodology. **Eliodoro Chiavazzo:** Writing – review & editing, Validation, Methodology. **Pietro Asinari:** Writing – review & editing, Validation, Supervision, Resources, Methodology. **Matteo Fasano:** Writing – review & editing, Validation, Supervision, Project administration, Methodology, Funding acquisition, Conceptualization.

Declaration of competing interest

The authors declare that they have no known competing financial interests or personal relationships that could have appeared to influence the work reported in this paper.

Acknowledgments

The authors acknowledge the project PaRaMetriC (21GRD03, *Metrological framework for passive radiative cooling technologies*), which received funding from the European Partnership on Metrology, co-financed by the European Union's Horizon Europe Research and Innovation Programme and from the Participating States.

Appendix A. Supplementary data

Supplementary material related to this article can be found online at https://doi.org/10.1016/j.energy.2025.139101.

Data availability

The complete dataset of model results is available open access in the associated Zenodo repository at https://doi.org/10.5281/zenodo.14938900.

References

[1] International Energy Agency. World energy outlook 2024. Paris: IEA; 2024.
[2] International Energy Agency. The future of cooling: Opportunities for energy-efficient air conditioning. Paris: IEA; 2018.
[3] Strobel Michael, Jakob Uli, Streicher Wolfgang, Neyer Daniel. Spatial distribution of future demand for space cooling applications and potential of solar thermal cooling systems. Sustainability 2023;15(12):9486.
[4] Copernicus Climate Change Service. 2024 is the first year to exceed 1.5 °C above pre-industrial level. 2025, URL https://climate.copernicus.eu/. [Retrieved 18 January 2025].
[5] International Energy Agency. Space cooling. 2023, URL https://www.iea.org/energy-system/buildings/space-cooling. [Retrieved 21 December 2024].
[6] Ritchie Hannah. Air conditioning causes around 3% of greenhouse gas emissions. How will this change in the future? Our world in data. 2024, https://ourworldindata.org/air-conditioning-causes-around-greenhouse-gas-emissions-will-change-future.
[7] Alberghini Matteo, Hong Seongdon, Marcelo Lozano L, Korolovych Volodymyr, Huang Yi, Signorato Francesco, et al. Sustainable polyethylene fabrics with engineered moisture transport for passive cooling. Nat Sustain 2021;4(8):715–24.
[8] Alberghini Matteo, Morciano Matteo, Fasano Matteo, Bertiglia Fabio, Fernicola Vito, Asinari Pietro, et al. Multistage and passive cooling process driven by salinity difference. Sci Adv 2020;6(11):eaax5015.
[9] Huang Jingyuan, Lin Chongjia, Li Yang, Huang Baoling. Effects of humidity, aerosol, and cloud on subambient radiative cooling. Int J Heat Mass Transfer 2022;186:122438.
[10] Ono Masashi, Chen Kaifeng, Li Wei, Fan Shanhui. Self-adaptive radiative cooling based on phase change materials. Opt Express 2018;26(18):A777–87.
[11] Bahadori Mehdi N. Passive cooling systems in iranian architecture. In: Renewable energy. 2018: Routledge; p. Vol1_87–101.
[12] Lu Xing, Xu Peng, Wang Huilong, Yang Tao, Hou Jin. Cooling potential and applications prospects of passive radiative cooling in buildings: The current state-of-the-art. Renew Sustain Energy Rev 2016;65:1079–97.
[13] Raman Aaswath P, Anoma Marc Abou, Zhu Linxiao, Rephaeli Eden, Fan Shanhui. Passive radiative cooling below ambient air temperature under direct sunlight. Nature 2014;515(7528):540–4.
[14] Wu Dong, Liu Chang, Xu Zenghui, Liu Yumin, Yu Zhongyuan, Yu Li, et al. The design of ultra-broadband selective near-perfect absorber based on photonic structures to achieve near-ideal daytime radiative cooling. Mater Des 2018;139:104–11.
[15] Rephaeli Eden, Raman Aaswath, Fan Shanhui. Ultrabroadband photonic structures to achieve high-performance daytime radiative cooling. Nano Lett 2013;13(4):1457–61.
[16] Zhai Yao, Ma Yaoguang, David Sabrina N, Zhao Dongliang, Lou Runnan, Tan Gang, et al. Scalable-manufactured randomized glass-polymer hybrid metamaterial for daytime radiative cooling. Science 2017;355(6329):1062–6.
[17] Huang Zhifeng, Ruan Xiulin. Nanoparticle embedded double-layer coating for daytime radiative cooling. Int J Heat Mass Transfer 2017;104:890–6.
[18] Kou Jun-long, Jurado Zoila, Chen Zhen, Fan Shanhui, Minnich Austin J. Daytime radiative cooling using near-black infrared emitters. Acs Photonics 2017;4(3):626–30.
[19] Mandal Jyotirmoy, Fu Yanke, Overvig Adam C, Jia Mingxin, Sun Kerui, Shi Norman N, et al. Hierarchically porous polymer coatings for highly efficient passive daytime radiative cooling. Science 2018;362(6412):315–9.
[20] Li Tian, Zhai Yao, He Shuaiming, Gan Wentao, Wei Zhiyuan, Heidarinejad Mohammad, et al. A radiative cooling structural material. Science 2019;364(6442):760–3.
[21] Pirvaram Atousa, Talebzadeh Nima, Leung Siu Ning, O'Brien Paul G. Radiative cooling for buildings: A review of techno-enviro-economics and life-cycle assessment methods. Renew Sustain Energy Rev 2022;162:112415.
[22] Zhao Bin, Hu Mingke, Ao Xianze, Chen Nuo, Pei Gang. Radiative cooling: A review of fundamentals, materials, applications, and prospects. Appl Energy 2019;236:489–513.
[23] Carlosena Laura, Ruiz-Pardo Álvaro, Feng Jie, Irulegi Olatz, Hernández-Minguillón Rufino J, Santamouris Mattheos. On the energy potential of daytime radiative cooling for urban heat island mitigation. Sol Energy 2020;208:430–44.
[24] Younes Jaafar, Ghali Kamel, Ghaddar Nesreen. Diurnal selective radiative cooling impact in mitigating urban heat island effect. Sustain Cities Soc 2022;83:103932.
[25] Bu Fan, Yan Da, Tan Gang, Sun Hongsan, An Jingjing. Systematically incorporating spectrum-selective radiative cooling into building performance simulation: Numerical integration method and experimental validation. Appl Energy 2022;312:118733.
[26] Chen Jianheng, Lu Lin. Comprehensive evaluation of thermal and energy performance of radiative roof cooling in buildings. J Build Eng 2021;33:101631.
[27] Feng Jie, Saliari Maria, Gao Kai, Santamouris Mattheos. On the cooling energy conservation potential of super cool roofs. Energy Build 2022;264:112076.
[28] Baniassadi Amir, Sailor David J, Ban-Weiss George A. Potential energy and climate benefits of super-cool materials as a rooftop strategy. Urban Clim 2019;29:100495.
[29] Wang Ningsheng, Lv Yinyan, Zhao Dongliang, Zhao Wenbo, Xu Jingtao, Yang Ronggui. Performance evaluation of radiative cooling for commercial-scale warehouse. Mater Today Energy 2022;24:100927.
[30] Yu Xinxian, Chen Chun. Coupling spectral-dependent radiative cooling with building energy simulation. Build Environ 2021;197:107841.
[31] Zghaib Peter, Es-Saidi Soukaina, Ortego Egoï, Rached Ghady Abou, Zoughaib Assaad. Deployment integration strategy for daytime radiative cooling materials: A comparative numerical analysis of roof cooling and water-cooling panels. In: EPJ web of conferences, vol. 309, EDP Sciences; 2024, p. 13002.
[32] Liu Junwei, Zhou Zhihua, Zhang Debao, Jiao Shifei, Zhang Ji, Gao Feng, et al. Research on the performance of radiative cooling and solar heating coupling module to direct control indoor temperature. Energy Convers Manage 2020;205:112395.
[33] Li Xiuqiang, Sun Bowen, Sui Chenxi, Nandi Ankita, Fang Haoming, Peng Yucan, et al. Integration of daytime radiative cooling and solar heating for year-round energy saving in buildings. Nat Commun 2020;11(1):6101.
[34] An Yidan, Fu Yang, Dai Jian-Guo, Yin Xiaobo, Lei Dangyuan. Switchable radiative cooling technologies for smart thermal management. Cell Rep Phys Sci 2022;3(10).
[35] Bergman Theodore L. Active daytime radiative cooling using spectrally selective surfaces for air conditioning and refrigeration systems. Sol Energy 2018;174:16–23.
[36] Goldstein Eli A, Raman Aaswath P, Fan Shanhui. Sub-ambient non-evaporative fluid cooling with the sky. Nat Energy 2017;2(9):1–7.
[37] SkyCool Systems. Reduced energy demand for cooling with the sky: Final report. Technical report, U.S. Department of Energy Advanced Research Projects Agency–Energy (ARPA-E); 2023, (Award No. AR0001251; Control No. 2039-1502).
[38] Yuan Jinchao, Yin Hongle, Cao Peng, Yuan Dan, Xu Shaoyu. Daytime radiative cooling of enclosed water using spectral selective metamaterial based cooling surfaces. Energy Sustain Dev 2020;57:22–31.
[39] Xu Dikai, Boncoeur Sébastien, Tan Gang, Xu Jingtao, Qian Hua, Zhao Dongliang. Energy saving potential of a fresh air pre-cooling system using radiative sky cooling. In: Building simulation, vol. 15, Springer; 2022, p. 167–78.
[40] Jeong Shin Young, Tso Chi Yan, Zouagui Mehdi, Wong Yuk Ming, Chao Christopher YH. A numerical study of daytime passive radiative coolers for space cooling in buildings. In: Building simulation, vol. 11, Springer; 2018, p. 1011–28.
[41] Zhang Kai, Zhao Dongliang, Yin Xiaobo, Yang Ronggui, Tan Gang. Energy saving and economic analysis of a new hybrid radiative cooling system for single-family houses in the USA. Appl Energy 2018;224:371–81.
[42] Fiorentini Massimo, Cooper Paul, Ma Zhenjun. Development and optimization of an innovative HVAC system with integrated PVT and PCM thermal storage for a net-zero energy retrofitted house. Energy Build 2015;94:21–32.
[43] González-Cruz Eduardo M, Krüger Eduardo L. Experimental study on a low energy radiant-capacitive heating and cooling system. Energy Build 2022;255:111674.
[44] Vilà Roger, Medrano Marc, Castell Albert. Numerical analysis of the combination of radiative collectors and emitters to improve the performance of water-water compression heat pumps under different climates. Energy 2023;266:126445.

[45] Hu Mingke, Zhao Bin, Li Jing, Wang Yunyun, Pei Gang. Preliminary thermal analysis of a combined photovoltaic–photothermic–nocturnal radiative cooling system. Energy 2017;137:419–30.
[46] Cola F, De Gennaro M, Perocchio D, Canuto E, Daniele S, Napoli P, et al. Integrated receivers with bottom subcooling for automotive air conditioning: Detailed experimental study of their filling capacity. Int J Refrig 2016;62:72–84.
[47] Hersbach H, Bell B, Berrisford P, Biavati G, Horányi A, Muñoz Sabater J, et al. ERA5 hourly data on pressure levels from 1940 to present, Copernicus Climate Change Service (C3S) Climate Data Store (CDS). 2023, [Retrieved 23 May 2024].
[48] The MathWorks Inc. Simscape (version 24.1). 2022, URL https://www.mathworks.com.
[49] Loga Tobias, Stein Britta, Diefenbach Nikolaus. Tabula building typologies in 20 european countries—making energy-related features of residential building stocks comparable. Energy Build 2016;132:4–12.
[50] Jankovic I, Fernandez X, Diriken J. Database of grey-box model parameter values for EU building typologies. Ambience EU Project Report, 2021.
[51] Nawaz Kashif, Shen Bo, Elatar Ahmed, Baxter Van, Abdelaziz Omar. R1234yf and R1234ze (E) as low-gwp refrigerants for residential heat pump water heaters. Int J Refrig 2017;82:348–65.
[52] Jia Linrui, Lu Lin, Gong Quan, Jiao Kai. Analytical and experimental analyses on cooling performances of radiative skycool radiators with various interior flowing channels. Energy 2024;295:130907.
[53] National Renewable Energy Laboratory. Reference air mass 1.5 spectra. 2023, URL https://www.nrel.gov/grid/solar-resource/spectra-am1.5.html. [Retrieved 5 November 2023].
[54] Das AK, Iqbal M. A simplified technique to compute spectral atmospheric radiation. Sol Energy 1987;39(2):143–55.
[55] Incropera Frank P, DeWitt David P, Bergman Theodore L, Lavine Adrienne S, et al. Fundamentals of heat and mass transfer, vol. 6. Wiley New York; 1996.
[56] Adibekyan A, Schumacher J, Pattelli Lorenzo, Manara Jochen, Meriç S, Bazkir Ö, et al. Emissivity and reflectivity measurements for passive radiative cooling technologies. Int J Thermophys 2025;46(5):1–16.
[57] Iacono Michael J, Delamere Jennifer S, Mlawer Eli J, Shephard Mark W, Clough Shepard A, Collins William D. Radiative forcing by long-lived greenhouse gases: Calculations with the aer radiative transfer models. J Geophys Res: Atmospheres 2008;113(D13).
[58] Mlawer Eli J, Taubman Steven J, Brown Patrick D, Iacono Michael J, Clough Shepard A. Radiative transfer for inhomogeneous atmospheres: Rrtm, a validated correlated-k model for the longwave. J Geophys Res: Atmospheres 1997;102(D14):16663–82.
[59] Zhao Dongliang, Aili Ablimit, Zhai Yao, Lu Jiatao, Kidd Dillon, Tan Gang, et al. Subambient cooling of water: toward real-world applications of daytime radiative cooling. Joule 2019;3(1):111–23.
[60] Dincer I, Rosen MA. Exergy analyses of refrigeration and heat pump systems. Exergy 2021;125–41.
[61] Yang Yujie, Zhang Guoqiang, Rong Li. Impact of cloud and total column water vapor on annual performance of passive daytime radiative cooler. Energy Convers Manage 2022;273:116420.
[62] Mokhtari Reza, Ulpiani Giulia, Ghasempour Roghayeh. The Cooling Station: Combining hydronic radiant cooling and daytime radiative cooling for urban shelters. 211, Elsevier; 2022, 118493,
[63] Peel Murray C, Finlayson Brian L, McMahon Thomas A. Updated world map of the Köppen-Geiger climate classification. Hydrol Earth Syst Sci 2007;11(5):1633–44.
[64] Huld Thomas, Paietta Elena, Zangheri Paolo, Pascua Irene Pinedo. Assembling typical meteorological year data sets for building energy performance using reanalysis and satellite-based data. Atmosphere 2018;9(2):53.
[65] Wu Yi, An Jingjing, Gui Chenxi, Xiao Chan, Yan Da. A global typical meteorological year (TMY) database on era5 dataset. In: Building simulation, vol. 16, Springer; 2023, p. 1013–26.
[66] Wu Xueke, Li Jinlei, Xie Fei, Wu Xun-En, Zhao Siming, Jiang Qinyuan, et al. A dual-selective thermal emitter with enhanced subambient radiative cooling performance. Nat Commun 2024;15(1):815.
[67] Peoples Joseph, Hung Yu-Wei, Li Xiangyu, Gallagher Daniel, Fruehe Nathan, Pottschmidt Mason, et al. Concentrated radiative cooling. Appl Energy 2022;310:118368.
[68] González-Cruz E, Pérez G, Borja F, Alonso C, Martin-Consuegra F, Krüger E, et al. Full-scale facility for the assessment of night and daytime passive radiative cooling. In: Proceedings of 2024 CATE conference. 20-22 November 2024 Seville, Spain, 2024, p. 179.
[69] Yadav Vinay Kumar, Gautam Kumar, Sarkar Jahar, Ghosh Pradyumna. Techno-economic assessment of novel solar-driven dual-mode trigeneration device featuring daytime radiative condenser. Energy 2025;137116.
[70] Song Jianing, Shen Qingchen, Shao Huijuan, Deng Xu. Anti-environmental aging passive daytime radiative cooling. Adv Sci 2024;11(10):2305664.
[71] He Yue, Lu Biao, Fang Jinzhong, Lei Yue, Gao Shan, Feng Chi. Radiative cooling for long-term building energy efficiency: an experimental comparison of seven coatings. Natl Sci Open 2024;3(3):20230065.
[72] Fan Fan, Xu Qihao, Zhao Dongliang. Heat transfer properties of dusty radiative cooling surface: Modeling and experimental studies. Int J Heat Mass Transfer 2023;214:124465.
[73] Chiatti Chiara, Marchini Francesco, Fabiani Claudia, Kousis Ioannis, Carlosena Laura, Pisello Anna Laura. Harnessing the potential of radiative cooling for the built environment: A new comprehensive protocol for materials' characterization. Sol Energy Mater Sol Cells 2024;277:113074.